

See discussions, stats, and author profiles for this publication at: <https://www.researchgate.net/publication/274900803>

First-Principles Modeling of a Dye-Sensitized TiO₂/IrO₂ Photoanode for Water Oxidation

ARTICLE in JOURNAL OF THE AMERICAN CHEMICAL SOCIETY · APRIL 2015

Impact Factor: 12.11 · DOI: 10.1021/jacs.5b02128 · Source: PubMed

CITATIONS

3

READS

35

2 AUTHORS:



Mariachiara Pastore

Italian National Research Council

50 PUBLICATIONS 1,201 CITATIONS

SEE PROFILE



Filippo De Angelis

Università degli Studi di Perugia

261 PUBLICATIONS 10,931 CITATIONS

SEE PROFILE

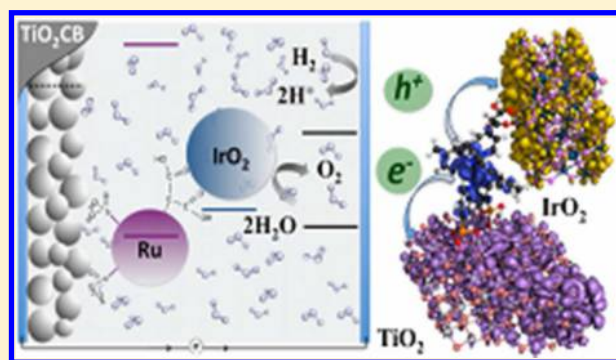
First-Principles Modeling of a Dye-Sensitized TiO₂/IrO₂ Photoanode for Water Oxidation

Mariachiara Pastore* and Filippo De Angelis*

Computational Laboratory for Hybrid Organic Photovoltaics (CLHYO), CNR-ISTM, via Elce di Sotto 8, I-06123 Perugia, Italy

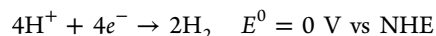
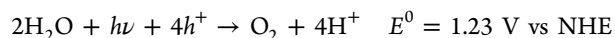
S Supporting Information

ABSTRACT: We present a first-principle computational modeling investigation, based on density functional theory (DFT) and time-dependent DFT, on the structural, electronic, optical, and charge generation properties of the semiconductor/dye/catalyst heterointerfaces in a prototypical dye-sensitized photoanode for water oxidation. The investigated architecture comprises a Ru(II) dye-sensitized TiO₂ substrate tethered to an IrO₂ nanoparticle catalyst. Our realistic modeling strategy and quantitative analysis of the relevant interfacial hole/electron transfer reactions indicates the slow hole injection into IrO₂ and the fast dye excited-state quenching to IrO₂ as the primary sources of the relatively poor cell efficiency experimentally observed. On the basis of this atomistic and electronic structure information, we propose and computationally test, against a prototype dye, a new class of Ru(II) sensitizers, which show potentially improved photoelectrochemical performances. This study constitutes a first step toward the computer-assisted design of new and more efficient materials for solar fuels production through dye-sensitized photoelectrochemical cells.



1. INTRODUCTION

One of the greatest scientific and technological challenges facing humanity is to capture and convert solar energy into electricity¹ or to store it into chemical fuels, producing hydrogen (or other reduced fuels) and oxygen from water.^{2–4} Solar hydrogen generation from water is a very attractive field of research, allowing the production of inexhaustible renewable fuel without emission of pollutants and greenhouse gases. The reactions taking place at the electrodes of a photoelectrochemical cell (PEC) are reported in the following, where h^+ and e^- are, respectively, the photogenerated holes and electrons:



The first example of a water splitting PEC was reported in 1972 by Fujishima and Honda.⁵ A semiconducting TiO₂ photoanode was irradiated with UV light, producing oxygen at the anode and hydrogen at a platinum cathode. Since this observation, over the last 40 years, the development of photocatalytic semiconducting metal oxides has represented a very active research field, with many reported systems showing high photocatalytic activities.^{6–8} The main limitation of these oxides is that they are only active under UV irradiation, thus exploiting only a minor fraction (ca. 4%) of solar power. The development of stable and highly efficient visible-light-driven photocatalysts has, therefore, represented a crucial issue in the attempt of enhancing semiconductor-based photocatalytic water splitting.^{9–14}

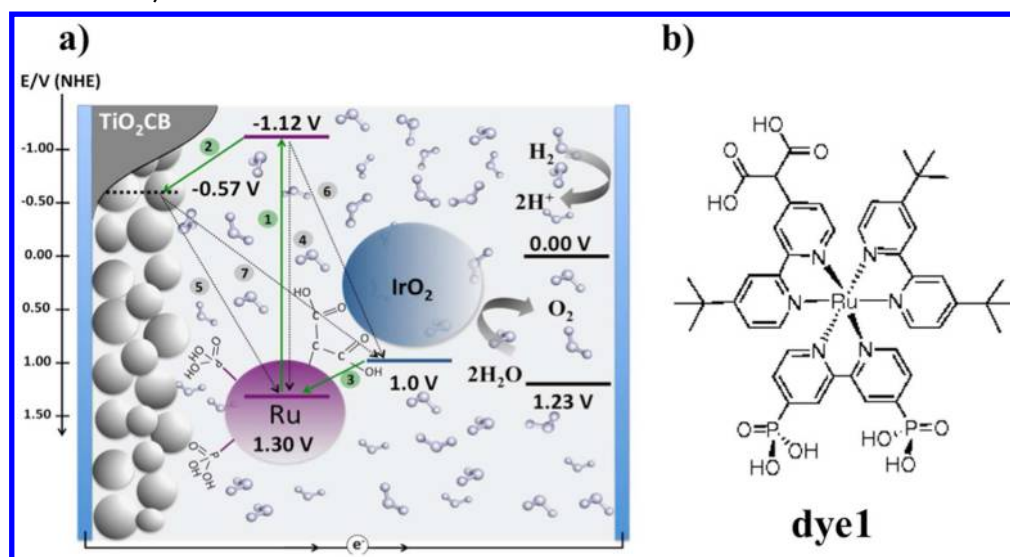
A different approach to visible-light water splitting relies on the use dye-sensitized semiconductor nanoparticles, linked to an oxygen evolving catalyst.^{15–24} In this type of PEC, directly related to the dye-sensitized solar cell, a dye adsorbed on the surface of a wide band gap semiconductor (typically TiO₂) absorbs the solar radiation to produce an electron and a hole, which are injected into the semiconductor and catalyst, respectively. In such a dye-sensitized PEC (DSPEC) oxygen is produced at the dye-sensitized semiconductor photoanode, while hydrogen is produced by a catalyst at the cathode, where photogenerated electrons are collected.

While the development of catalysts and sensitizers for the proton reduction half reaction has achieved a significant progress over the last years,²⁵ the four-electron water oxidation reaction represents the main barrier toward the design of efficient and stable water splitting devices. Individual characteristics of water oxidation catalysts (WOCs), photosensitizers, and semiconductors as well as the interfacial properties of the assembled photoanodes strongly interplay in determining the quantum (percentage conversion of photons to hole–electron pairs) and Coulombic (percentage conversion of 4 hole–electrons pairs into O₂ molecules) efficiencies.² Both molecular^{26–37} and heterogeneous metal-oxide^{38–42} WOCs have been reported so far. Molecular (homogeneous) WOCs, while offering the advantages of a larger structural variability and of an easier kinetic and mechanistic characterization, are often unstable and labo-

Received: February 27, 2015

Published: April 13, 2015

Scheme 1. (a) Scheme of a Prototypical DSPEC¹⁶ along with Main Energy Levels and Relevant Electron Transfer Processes^a and (b) Molecular Structure of Dye1



^a(1) Dye photoexcitation; (2) electron injection/semiconductor reduction; (3) hole injection/catalyst oxidation; (4) dye radiative or nonradiative recombination; (5) electron–hole recombination to the oxidized dye; (6) oxidative dye excited-state quenching to the catalyst; (7) electron–hole recombination to the oxidized catalyst.

rious to synthesize. On the other hand, metal-oxide nanoparticle WOCs, such as RuO₂ and IrO₂, are synthetically easy to obtain and generally stable, although their structural and operational characterization is not straightforward. Iridium oxide, both in its crystalline (IrO₂) and amorphous colloidal (IrO₂·*n*H₂O) form, is a central player in the development of photoanodes for water oxidation.^{15,16,21,43–48} This unsurpassed success, only recently matched by optimized perovskite transition metal oxides,⁴⁹ is mainly due to its relatively low overpotential for water oxidation (0.2–0.3 V) over a large pH range with a high turnover frequency (TOF) of 40 s^{−1}.¹⁷ The sensitizing dye characteristics are also central to the DSPEC efficiency. Optimal dyes should possess: (i) wide and intense absorption in the visible and possibly near-infrared region; (ii) sufficiently long-lived charge separated excited state to inject the photoexcited electrons into the conduction band (CB) semiconductor; and (iii) appropriate redox potential to sustain the catalytic water oxidation along with stable anchoring to the semiconductor surface in the oxidative PEC environment.

To date, the most widely employed DSPEC sensitizers are [Ru(bpy)₃]²⁺ derivatives⁵⁰ or porphyrin-based compounds,^{51–53} properly modified to be effectively grafted on water splitting photoanodes. On the semiconductor side, due to the instability of ZnO in acidic conditions, mesoporous TiO₂ or hybrid core–shell ZnO–TiO₂ and CdSe/TiO₂ nanostructures are the materials of choice.^{17,42,54,55} Despite substantial research efforts, the effective integration of sensitizers, WOCs and semiconductors into efficient photoanodes for water oxidation is still a challenge, and only few complete systems have been reported so far.^{15,18,19,20,21,34,56,57,58} The first assembled molecular photoanode was reported in 2009 by Mollouk and co-workers,¹⁵ employing a bifunctional heteroleptic Ru(II) sensitizer, showing phosphonate groups for TiO₂ anchoring, and a malonate group to bind to hydrated iridium oxide (IrO₂·*n*H₂O) nanoparticles (dye1 in Scheme 1).

As schematically depicted by the green arrows in Scheme 1, the forward intramolecular and interfacial hole/electron transfer

processes occurring at the photoanode (besides the four electron water oxidation process) are:

- | | |
|--|--|
| 1) Dye + <i>hν</i> → Dye* | (dye photoexcitation) |
| 2) Dye* + TiO ₂ → Dye(<i>h</i> ⁺) + TiO ₂ (<i>e</i> [−]) | (electron injection/semiconductor reduction) |
| 3) Dye(<i>h</i> ⁺) + IrO ₂ → Dye + IrO ₂ (<i>h</i> ⁺) | (hole injection/catalyst oxidation) |

The parasitic processes contributing to decrease the DSPEC efficiency, represented by dotted gray arrows in Scheme 1, are instead:

- | | |
|--|---|
| 4) Dye* → Dye + energy | (dye radiative or non radiative recombination) |
| 5) TiO ₂ (<i>e</i> [−]) + Dye(<i>h</i> ⁺) → TiO ₂ + Dye | (electron–hole recombination to the oxidized dye) |
| 6) Dye* + IrO ₂ → Dye(<i>h</i> ⁺) + IrO ₂ (<i>e</i> [−]) | (oxidative dye excited state quenching to the catalyst) |
| 7) TiO ₂ (<i>e</i> [−]) + IrO ₂ (<i>h</i> ⁺) → TiO ₂ + IrO ₂ | (electron–hole recombination to the oxidized catalyst) |

Under light irradiation, this type of DSPEC produced both oxygen and hydrogen, even if low internal quantum yield and Coulombic efficiency (about 0.9% and 20%, respectively) were reported.¹⁵ The non optimal device performances were mainly attributed to a slow hole transfer from the oxidized dye to the catalyst (process 3), which in turn favored a high back recombination from TiO₂ to the oxidized dye (process 5). A fast dye's excited-state quenching by IrO₂·*n*H₂O has also been envisioned⁵⁹ as a possibly additional deactivation channel. Incorporation of a biomimetic electron mediator between the catalyst and the dye was found to enhance the hole transfer rate between Ru(III) and Ir(IV), determining a 3-fold increase in the photoanode efficiency.²¹ Recently, with the aim of increasing the photocatalytic activity per surface iridium atom, the carboxylic-phosphonic capping of the (IrO₂·*n*H₂O) nanoparticles was eliminated by directly sintering the catalyst onto the TiO₂ surface;^{46,48} the proposed architecture, however, suffered of fast TiO₂(*e*[−]) to IrO₂(*h*⁺) recombination, cf. process 7).

This analysis draws out the key problems in this kind of device: (i) the structural, electronic, and charge transfer properties of the semiconductor/dye/WOC interfaces; (ii) stable adsorption and coadsorption, with an optimal ratio, of dye and catalyst or dye–catalyst assemblies⁶⁰ on the oxide surface; and (iii) the energy

level matching and electronic coupling, influencing the kinetics of the forward and backward electron transfers.

Computational modeling has had a great impact in dye-sensitized solar cells technology. Simulation of isolated device components as well as of the relevant interfaces ruling the devices operational mechanisms has successfully supported experimental research by providing molecular design rules of new materials and a deeper understanding of the chemical and physical processes governing the complex cell interfaces.^{61,62} A comparable understanding of DSPEC is still lacking, especially for what concerns the interfacial (e^-/h^+) transfer phenomena, which are central to the efficient device functioning. Most of previous computational modeling studies, indeed, focused on the characterization of the water oxidation reaction mechanism,^{63–67} with only a few investigations devoted to the interaction between the WOC and the semiconductor.^{26,68}

With the aim of providing the fundamental understanding underlying the rate of the forward (e^-/h^+) transfer processes and effectively suppressing the undesired parasitic recombination reactions, here we report a fully first-principles modeling of a DSPEC photoanode comprising a ruthenium dye-sensitized TiO_2 model tethered to an IrO_2 nanoparticle catalyst. To our knowledge, this is the first computational study to address the nature of IrO_2 nanoparticles and to model their use as catalysts in a DSPEC. Based on such realistic model, we investigate all the relevant interfacial (e^-/h^+) transfers by hybrid DFT calculations in solution, determining the interplay of structural and electronic factors affecting the DSPEC efficiency. With this information at hand, we design a novel class of Ru(II) sensitizers rooted onto sound and documented synthetic chemical strategies, and we computationally investigate their performance in a DSPEC architecture against the parent dye1, see Scheme 1. Rewardingly, our results for the new dye show potentially improved photo-electrochemical performances, casting the desired design rules for new and more efficient devices.

2. COMPUTATIONAL DETAILS

Based on our previous expertise, TiO_2 was modeled by a neutral stoichiometric $(\text{TiO}_2)_{82}$ cluster of ca. 2×2 nm side, obtained by appropriately “cutting” an anatase slab exposing the majority (101) surface.^{69,70} This cluster model allows us to employ hybrid functionals and continuum solvation models, providing energy levels in close agreement with experimental band edges of anatase TiO_2 .^{71,72} To our knowledge, IrO_2 nanoparticles have never been simulated. After testing various models, all extracted from a rutile (110) surface slab cut from the bulk, we opted for a $\text{Ir}_{56}\text{O}_{114}\text{H}_4$ neutral cluster, formally $(\text{IrO}_2)_{56} \cdot 2\text{H}_2\text{O}$, which represented a good compromise between system dimensions (ca. $1 \times 1 \times 0.5$ nm) and accuracy in the structural (majority (110) rutile surfaces), electronic (band edges), and optical (UV–vis) properties of experimentally characterized IrO_2 systems, see below.

Ground-state equilibrium geometry of stand-alone dyes, IrO_2 and TiO_2 models as well as dye- TiO_2 , dye- IrO_2 and $\text{TiO}_2/\text{dye}/\text{IrO}_2$ assemblies were optimized in the gas phase with the ADF program package,⁷³ using the Becke–Perdew exchange–correlation functional^{74,75} and a double- ζ basis set. DFT electronic structure and TDDFT excited-state calculations in water solution were carried out on the optimized systems using the hybrid B3LYP functional together with a polarizable continuum model of solvation (C-PCM)^{76,77} as implemented in the Gaussian09 suite of programs.⁷⁸ Single point calculations on the $\text{TiO}_2/\text{dye}/\text{IrO}_2$ and on the smaller dye- TiO_2 and dye- IrO_2 assemblies were performed employing a 6-311G** basis set for the dye atoms, with the LanL2 pseudopotential for Ru, a LanL2DZ basis set, and pseudopotentials^{79–82} for the IrO_2 nanoparticle and a 3-21G* basis set for TiO_2 , which was previously shown to deliver accurate excited-state energy levels for dye-sensitized TiO_2 .^{71,72} TDDFT excited-state calculations for the dye- TiO_2 and dye- IrO_2 assemblies were

performed with a 3-21G* and with LanL2DZ basis and pseudopotential, respectively, thus using a smaller basis set for the dye only compared to the larger assemblies for computational convenience.

To evaluate the electronic coupling between the dye's, semiconductor, and catalyst electronic states and thus to estimate the associated injection rates, we resorted to a Fermi golden rule framework, where the (e^-/h^+) injection rate k_{inj} is defined as

$$k_{inj} = \frac{2\pi}{\hbar} \sum_k |V_{dk}|^2 \rho(\epsilon_k) \quad (1)$$

where the k sum runs over the manifold of TiO_2 or IrO_2 acceptor states of interest and d is the dye donor state. The $|V_{dk}|^2 \rho(\epsilon_k)$ product is the probability distribution $\Gamma(\epsilon_k)$. The inverse of k_{inj} is the injection time τ . To evaluate the diabatic states needed to calculate the coupling matrix elements V_{dk} and partial density of states (DOS) $\rho(\epsilon_k)$, we adopted the model proposed by Thoss et al.^{83,84} and recently applied to the dye/ TiO_2 interfaces in dye-sensitized solar cells.^{85,86} This approach is based on the localization of the molecular orbitals of the entire complex on the donor and acceptor species, resulting in a block Fock matrix of the interacting system, where the diagonal elements represent the energies of the localized states, while the off-diagonal blocks contain the state to state coupling elements.

We evaluated the electronic coupling and the transfer rates, for the following processes, labeled according to Scheme 1: 2) electron injection from the dye excited state to the TiO_2 slab; 6) the dye excited-state quenching arising from electron injection to the IrO_2 catalyst; 3) the hole transfer from the oxidized dye to the IrO_2 catalyst; and 5) the electron/hole recombination from TiO_2 to the oxidized dye. Processes 2) and 6) were modeled by calculating the electronic coupling between the dye LUMO and the TiO_2 and IrO_2 manifold of unoccupied states on the dye- TiO_2 and dye- IrO_2 systems, respectively; process 3) was analyzed in the dye- IrO_2 complex, by evaluating the coupling elements between the dye HOMO and the IrO_2 manifold of occupied states; and process 5) was investigated by calculating the electronic coupling between the dye HOMO and the TiO_2 CB states on the dye- TiO_2 system. We note that, with the energy alignment shown in Scheme 1, the only process that were able to model using the complete $\text{TiO}_2/\text{dye}/\text{IrO}_2$ assembly, partitioned into IrO_2 and dye- TiO_2 subsystems, was the hole transfer from the dye HOMO to the IrO_2 catalyst.

3. RESULTS AND DISCUSSION

3.1. Modeling the DSPEC Building Blocks: The Isolated TiO_2 , Dye, and IrO_2 Systems. The band offset energetics between the dye and the $\text{TiO}_2/\text{IrO}_2$ oxides play a fundamental role, along with the coupling matrix elements, in determining the rate of (e^-/h^+) transfer reactions, cf. eq 1. Prior to discussing the results for the combined $\text{TiO}_2/\text{dye}/\text{IrO}_2$ assemblies, we thus benchmark our computational methodology against available experimental electronic and optical data for the isolated TiO_2 , dye and IrO_2 systems.

The electronic properties of isolated ruthenium dyes in solution are a clear success case of DFT/TDDFT methods employing hybrid functionals.^{62,72} Similarly, TiO_2 clusters of reasonably large dimensions have been shown to accurately reproduce the structural and electronic features of extended TiO_2 surfaces.^{62,71,72} The electronic structure and optical properties of IrO_2 have been widely investigated both experimentally and theoretically,^{87–91} although to the best of our knowledge no IrO_2 nanoparticles have been computationally modeled so far. We thus briefly report on the new model proposed here, $(\text{IrO}_2)_{56} \cdot 2\text{H}_2\text{O}$, whose structure is reported in Figure 1. IrO_2 crystallizes in the rutile structure, which is retained by our model exposing the majority (110) surfaces, where the degeneracy of the Ir 5d orbitals is lifted by the typical e_g/t_{2g} crystal field splitting.⁹² A comparison between the experimental XPES spectrum for bulk IrO_2 (clean surface) and the calculated valence DOS of our

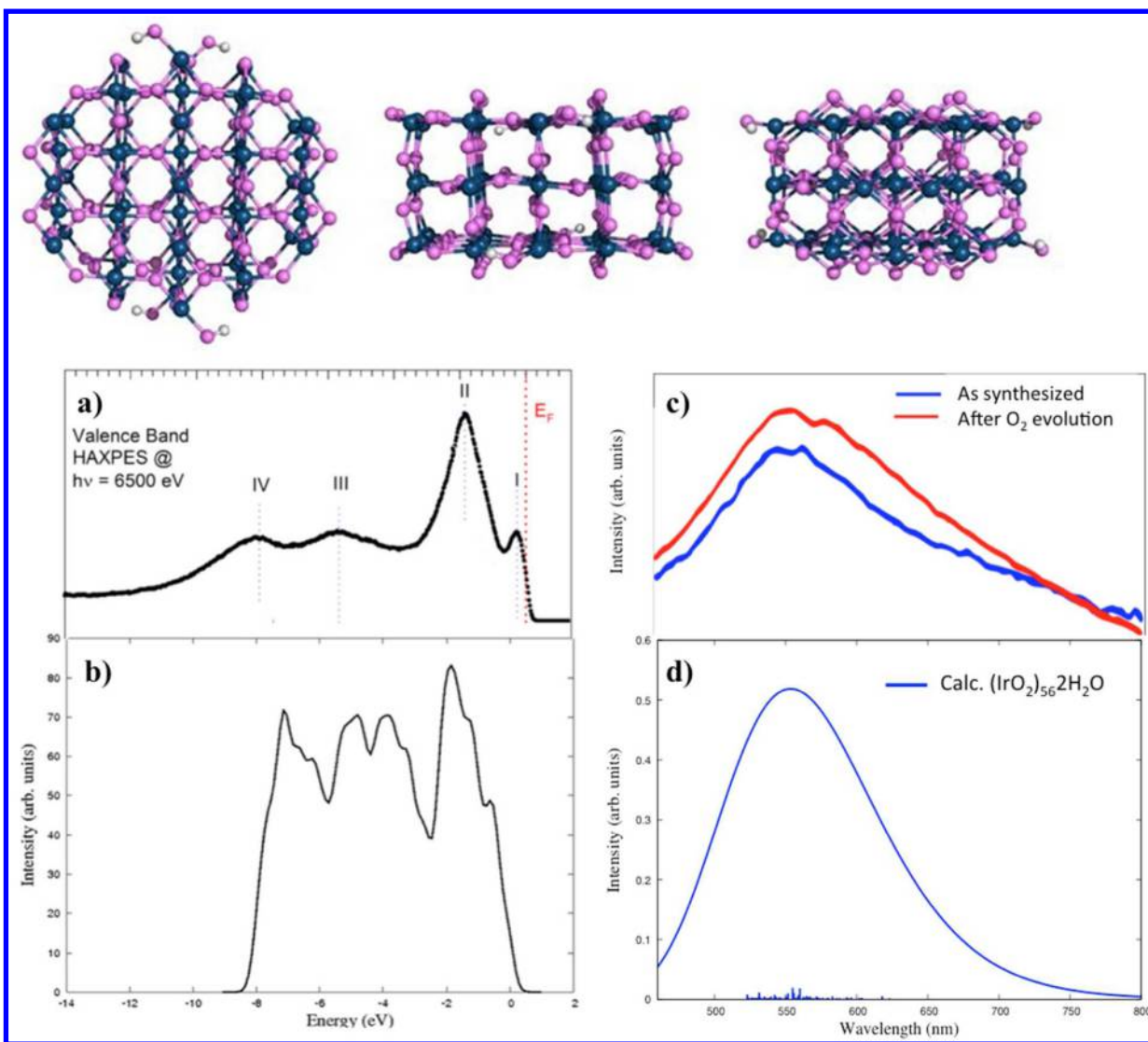


Figure 1. Top: Optimized structure of the (IrO₂)₅₆·2H₂O nanoparticle model along different views. Dark blue: Ir; magenta: O; white: H atoms. Bottom: (a) Experimental HAXPES spectrum of the IrO₂ valence band adapted from ref 91. (b) Calculated valence DOS of the (Ir₅₆O₁₁₂·2H₂O) nanoparticle. (c) Experimental UV–vis absorption spectrum of 2 nm IrO₂ nanoparticles in water solution from ref 95. (d) TDDFT-calculated UV–vis absorption spectrum of the (Ir₅₆O₁₁₂·2H₂O) nanoparticle in water. Vertical sticks represent calculated transition wavelengths and oscillator strengths.

model nanoparticle is reported in Figure 1a,b, respectively, showing that the (IrO₂)₅₆·2H₂O model well reproduces the overall electronic structure of the extended system: the main features of the valence band (labeled as II, III, and IV) are rather precisely predicted as well as the small feature (I) in the correspondence of the Fermi level.^{91,93} The (IrO₂)₅₆·2H₂O HOMO (VB edge) is calculated at -5.58 eV, while the CB edge is found at -5.09 eV. The small energy gap is consistent with the metallic nature of IrO₂, with the band gap opening possibly related to quantum confinement in our model nanoparticle. We thus estimate an oxidation (reduction) potential of 1.14 (0.65) V vs NHE (calculated values obtained against the vacuum are reported to the NHE scale by addition of 4.44), which nicely matches the voltammetry data measured for 2 nm IrO₂ nanoparticles in water solution, ranging from 0.9 (\approx pH = 7) to 1.1 V (\approx pH = 2).⁹⁴ We also calculated by TDDFT several low-lying transitions associated with the visible absorption band of the IrO₂ nanoparticle, mainly corresponding to the $t_{2g} \rightarrow e_g$ transitions of the Ir(IV) cation in the distorted octahedral coordination. We find an absorption maximum at 553 nm, Figure 1d)

in excellent agreement with the experimental absorption at ~ 550 – 570 nm, Figure 1c, with a tail down to 800 nm.⁹⁵

A summary of the relevant energy levels for the isolated DSPEC components is reported in Table 1 against known experimental quantities. As it can be noticed, the combination of hybrid DFT/TDDFT values calculated in solution satisfactorily reproduces the experimental energy levels of the dye, TiO₂, and IrO₂, making us confident of the accuracy of the employed methodological setup.

3.2. Modeling the DSPEC Photoanode: The TiO₂-Dye, Dye-IrO₂, and Tethered TiO₂/Dye/IrO₂ Assemblies. The adsorption of ruthenium polypyridyl complexes on the anatase (101) TiO₂ surface by phosphonic acidic groups has been investigated both experimentally^{97–102} and theoretically,^{103–105} as this anchoring group tends to give stronger binding to metal oxide surfaces, guaranteeing better long-term stability, compared to carboxylic acid groups. The precise binding mode of phosphonic acid to the TiO₂ surface is still to be unequivocally assessed experimentally,^{106–108} with theoretical works pointing to either monodentate^{104,109} or bidentate bridging modes.^{103,110–112}

Table 1. Ground-State Oxidation and Reduction Potential Calculated Using the Koopman's Theorem ($-\epsilon_{\text{HOMO}}$) and ($-\epsilon_{\text{LUMO}}$), Respectively, Along with Excited-State Oxidation Potential Obtained Adding the $S_0 \rightarrow S_1$ Vertical Excitation Energy to ($-\epsilon_{\text{HOMO}}$)^a

| system | calc. data | | exp. data | |
|------------------|--------------------|----------------------------|--------------------------|--------------------------|
| | HOMO | LUMO/LUMO* | HOMO | LUMO/LUMO* |
| dye1 | -5.96 ^b | -2.62/-3.53 ^b | -5.74 ^d | -3.24 ^d |
| IrO ₂ | -5.58 ^b | -5.09/-3.94 ^b | -5.34/-5.54 ^e | -5.04/-4.64 ^e |
| TiO ₂ | -7.25 ^b | -3.28/-3.76 ^{b,c} | -7.04 | -3.84 ^f |

^aAll values are in eV. Experimental data (V vs NHE) are converted in eV against the vacuum by adding 4.44. ^bThis work. ^cRef 71. ^dRef 34 for [Ru(bpy)₂(bpy-PO₃H₂)₂]²⁺. ^eRef 94. ^fRef 96.

Here we consider the dye interacting with the TiO₂ surface in its partially deprotonated form (2H), ensuring an overall neutral system, with both the phosphonate groups binding via a bidentate anchoring with one hydrogen bond to a surface oxygen atom (Figure 2a), similar to the results of ref 103. The interaction between the phosphonate groups and the anatase surface is rather strong, with O...Ti distances (symmetrical in the two anchoring groups) of 1.98 and 2.12 Å, the latter larger value corresponding to the Ti atom adjacent to the surface oxygen interacting via hydrogen bond with the dye.

On the other side, the dye is tethered to the (IrO₂)₅₆·2H₂O nanoparticle by a bidentate anchoring through a malonic acid group⁵⁹ (Figure 2b), with calculated Ir...O distances of 2.20 and 2.23 Å. When considering the TiO₂/dye/IrO₂ assembly, Figure 2c, the system retains the geometry of the separated TiO₂-dye and dye-IrO₂ assemblies, leading to an almost orthogonal arrangement of the TiO₂ and IrO₂ surfaces, Figure 2c. We notice that in principle the malonate group used for IrO₂ anchoring could bind TiO₂, and similarly the TiO₂-binding phosphonate groups may interact with IrO₂. While for simplicity we did not consider this "reverse" situation, we believe it might lead to unwanted parasitic excited-state quenching phenomena.

The electronic structure of the TiO₂/dye1 interface, Figure 3, presents the typical energy level alignment of Ru(II)-polypyridyl sensitized TiO₂.^{72,113} The three almost degenerate HOMOs are mainly localized on the dye and are practically identical to those of

the fully protonated isolated molecule, by virtue of the interaction of the anionic phosphonate groups with the TiO₂ substrate. A significant broadening of the dye LUMO is calculated, which extends ~0.5 eV above the energy of the TiO₂ CB bottom over a range of ~2 eV. This picture is suggestive of strongly coupled electronic states, inducing fast electron injection.

When dye1 is tethered to the IrO₂ catalyst, three almost pure dye HOMOs are recognizable at ~0.6–0.7 eV below the IrO₂ VB edge, i.e., essentially at the same energy they have in the isolated dye. This energy difference represents the maximum driving force for hole injection into IrO₂. The reduced interaction between the dye1 HOMOs and the IrO₂ VB, as inferred by the negligible HOMOs broadening in the dye-IrO₂ assembly, is an indication of the weak electronic coupling associated with the dye → IrO₂ hole transfer process.¹⁵ The dye LUMO broadening upon interaction with the IrO₂ CB states, even if considerably weaker than that observed in the TiO₂-dye assembly, is still appreciable. These latter data are in line with the measured efficient excited-state quenching observed for IrO₂-bound sensitizers.⁵⁹

The calculated UV-vis absorption spectra of the isolated, TiO₂- and IrO₂-bound dye1, see Figure 4, quantitatively compare with the experimental UV-vis spectra reported by Youngblood et al.¹⁵ The absorption maximum for dye1, associated with the typical metal to ligand charge transfer (MLCT) transition, is predicted at 443 nm, and it is red-shifted to 479 nm when the sensitizer is tethered to the IrO₂ catalyst; a slight red-shift is also observed in the experimental spectra, where the maximum for the unbound dye is found at ca. 465 nm, which can be related to the IrO₂-induced broadening of the dye LUMO. A small shift at longer wavelengths (459 nm) is also computed for the dye-sensitized TiO₂, see Figure 4.

3.3. Interfacial Electron and Hole Transfer Reactions.

Based on the electronic structure picture discussed above, we calculated the rates of the relevant (e^-/h^+) transfer process, namely:

| | |
|---|---|
| 2) Dye* + TiO ₂ → Dye (h ⁺) + TiO ₂ (e ⁻) | (electron injection/semiconductor reduction) |
| 3) Dye (h ⁺) + IrO ₂ → Dye + IrO ₂ (h ⁺) | (hole injection/catalyst oxidation). |
| 5) TiO ₂ (e ⁻) + Dye (h ⁺) → TiO ₂ + Dye | (electron-hole recombination to the oxidized dye) |
| 6) Dye* + IrO ₂ → Dye (h ⁺) + IrO ₂ (e ⁻) | (oxidative dye excited state quenching to the catalyst) |

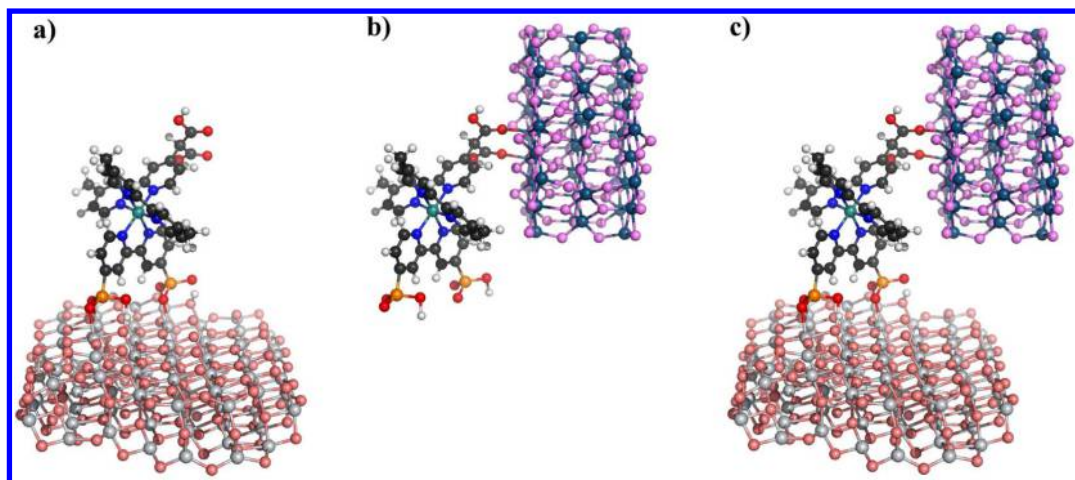


Figure 2. Optimized molecular structure of dye1 in its partially deprotonated form (2H), grafted to the (TiO₂)₈₂ cluster (a), to the (IrO₂)₅₆·2H₂O nanoparticle (b), and tethered across the TiO₂ and IrO₂ systems, (c). Dark blue: Ir; magenta: O (IrO₂); white: H atoms; light gray: Ti; pink: O (TiO₂); dark gray: C; red: O (dye); cyan: Ru; blue: N; orange: P.

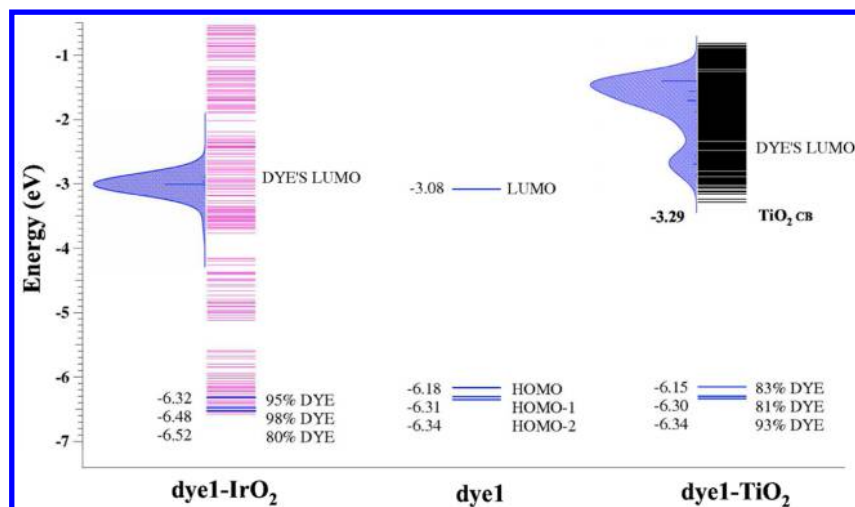


Figure 3. Alignment of energy levels for dye1 at TiO₂/dye and dye/IrO₂ interfaces compared to the energy levels of the stand-alone dye. Dye, IrO₂, and TiO₂ levels are in blue, magenta, and black colors, respectively. The percentages of dye contributions to the HOMOs of TiO₂/dye and dye/IrO₂ assemblies are also reported.

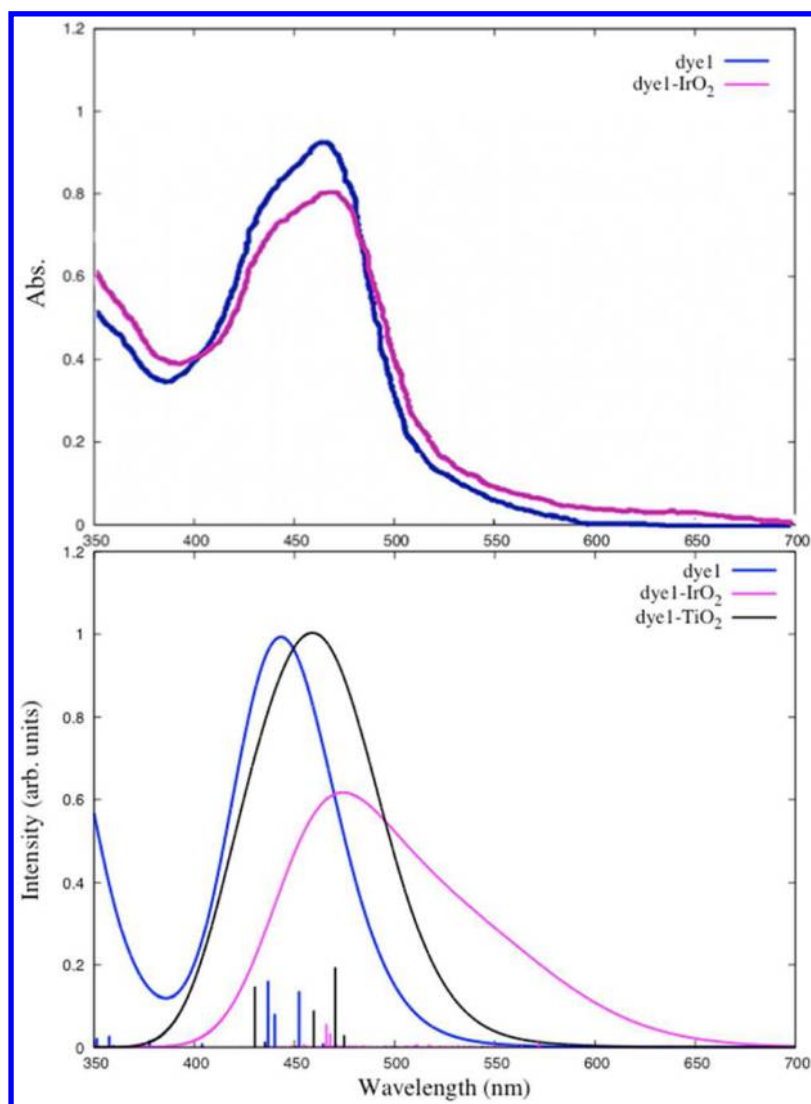


Figure 4. Comparison between the experimental, top, and calculated, bottom, UV-vis absorption spectra of the isolated dye1 in solution and of the TiO₂/dye and dye/IrO₂ interfaces. Experimental data from ref 15.

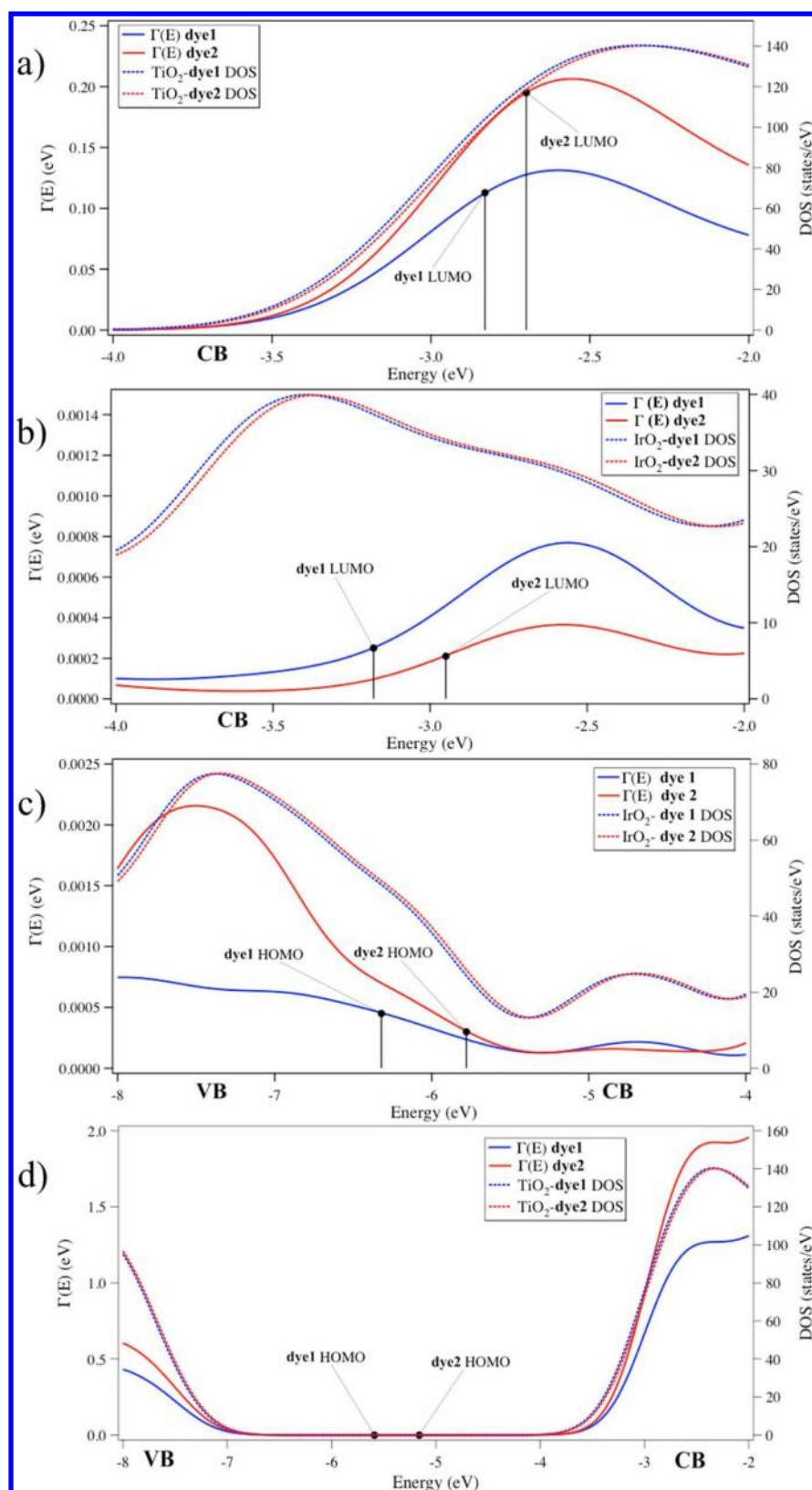


Figure 5. Probability distribution $\Gamma(\epsilon_k)$ (left scale, solid line, eV) and diatomic DOS (right scale, dashed line, eV^{-1}) for: (a) electron injection from the dye LUMO to the TiO_2 CB (process 2); (b) the oxidative dye excited-state quenching to the IrO_2 CB (process 6); (c) the hole injection from the dye to the IrO_2 VB (process 3); and (d) the electron/hole recombination from the TiO_2 CB to the oxidized dye (process 5). The relevant dye energy levels are also reported. Results for dye1 (dye2) are in blue (red) colors.

The results for processes 2, 3, 6, and 5 are reported in Figure 5a–d in terms of probability distribution $\Gamma(\epsilon_k)$ and

diatomic density of acceptor states, either TiO_2 or IrO_2 , $\rho(\epsilon_k)$, cf. eq 1, along with the relevant dye energy levels; the $\Gamma(\epsilon)$ values

extracted at the diabatic dye HOMO/LUMO values, along with the associated calculated injection rates are collected in Table 2, while their comparison with a set of available experimental data is

Table 2. Probability Distributions, Γ (eV) and DOS (number of states/eV) Calculated at the Diabatic HOMO and LUMO Energies and Associated Injection Rates, k_{inj} (s^{-1})

| | Γ (eV) | DOS (states/eV) | k_{inj} (s^{-1}) |
|---|-----------------------|----------------------|------------------------|
| $Dye^* + TiO_2 \rightarrow Dye^+ + TiO_2 (e^-)$ | | | |
| dye1-TiO ₂ | 0.1128 | 106 | 1.6×10^{14} |
| dye2-TiO ₂ | 0.1940 | 117 | 3.3×10^{14} |
| $Dye^* + IrO_2 \rightarrow Dye^+ + IrO_2 (e^-)$ | | | |
| dye1-IrO ₂ | 2.5×10^{-4} | 37 | 3.3×10^{11} |
| dye2-IrO ₂ | 1.2×10^{-4} | 34 | 2.0×10^{11} |
| $IrO_2 + Dye (h^+) \rightarrow IrO_2 (h^+) + Dye$ | | | |
| dye1-IrO ₂ | 4.5×10^{-4} | 48 | 1.0×10^{12} |
| dye2-IrO ₂ | 3.0×10^{-4} | 26 | 5.0×10^{11} |
| TiO ₂ -dye1-IrO ₂ | 2.7×10^{-4} | 45 | 0.5×10^{11} |
| TiO ₂ -dye2-IrO ₂ | 4.6×10^{-4} | 37 | 1.0×10^{12} |
| $TiO_2 (e^-) + Dye (h^+) \rightarrow TiO_2 + Dye$ | | | |
| dye1-TiO ₂ | 6.3×10^{-11} | 1.5×10^{-9} | 1.0×10^4 |
| dye2-TiO ₂ | 1.2×10^{-11} | 5.3×10^{-9} | 2.0×10^3 |

reported in Supporting Information. We notice that in principle these calculations should be performed at the relaxed geometry of the adsorbed dye in either its excited or oxidized state (neglecting relaxation of TiO₂/IrO₂ upon reduction/oxidation, which is expected to be quite small). For electron injection to TiO₂, i.e., process 2, a vertical approximation is usually valid due to the ultrafast (\sim fs) time scale of this phenomenon. The problem thus mainly involves the hole injection from the oxidized dye to the IrO₂ catalyst, process 3, and the excited-state quenching, process 6. To estimate the entity of geometrical relaxation, we have calculated the optimized geometry of the oxidized dye and found only a minimal geometrical relaxation from its ground-state optimized geometry, amounting to only 0.18 eV. The small relaxation energy suggests that a comparably small geometrical relaxation occurs, thus justifying the use of the ground-state geometry.

As it can be noticed from Figure 5 and Table 2, the fastest process (highest k) is the electron injection from the dye LUMO to the TiO₂ CB, which is predicted to occur on the fs time scale, in agreement with the experimental <100 fs dynamics observed for this process.¹¹⁴ For dye1, the hole injection from the dye HOMO to the IrO₂ VB is about 3 orders of magnitude less efficient, compare Figure 5a,c and injection rates in Table 2. The rate of the parasitic oxidative dye excited-state quenching to IrO₂ is comparable to that of hole injection for dye1, compare Figure 5b,c. Notably, in agreement with the ms experimental time scale (Supporting Information), recombination to the oxidized dye is calculated to be an extremely slow process, Figure 5d, due to the negligible energetic overlap between the dye HOMO and the TiO₂ CB (poor DOS of acceptor states).

The quantitative picture extracted from our calculations clearly highlights the problems associated with the functioning of the DSPEC based on dye1, i.e., despite a typically fast electron injection into TiO₂, a slow hole injection into IrO₂, and a comparable rate of IrO₂ reduction by the photoexcited dye are indeed predicted. The reasons underlying this electron/hole transfer picture can be qualitatively understood by looking at the charge density difference occurring upon photoexcitation in dye1, Figure 6c. While the excited electron is delocalized on the

acceptor bipyridines bound to TiO₂ through the phosphonate groups, the hole mainly resides on the ruthenium center with a negligible delocalization towards the malonate-functionalized bipyridine through which the dye is anchored to IrO₂. This electron/hole localization also explains why the “reverse” anchoring discussed above, with the phosphonate groups binding to IrO₂, may be harmful for the DSPEC efficiency, carrying the photoexcited electron closer to the IrO₂ thus possibly enhancing the excited-state quenching.

Based on this analysis and inspired by the electronic structure of ruthenium-based solar cells photosensitizers, we sought to introduce a modification into the chemical structure of dye1 which could accomplish at the same time a delocalization of the dye HOMO toward the IrO₂-anchoring malonate-functionalized bipyridine and a concomitant shift of the relevant LUMO away from the malonate-functionalized bipyridine, to enhance and suppress, respectively, hole and electron transfer to the IrO₂ nanoparticle. To our eyes, the most straightforward way to engineer this sensitizer modification is to introduce a malonate-functionalized cyclometalated phenylpyridine moiety in place of the bipyridine used for IrO₂ anchoring, see dye2 structure in Figure 6b. Cyclometalated Ru(II) complexes have been successfully applied as solar cell sensitizers in the dye-sensitized solar cells,^{115–119} as they present conveniently tunable HOMOs and LUMO levels and a broad and red-shifted absorption spectrum at same time. Functional to our target, the spatial localization of the HOMO is partly shifted in this class of compounds from the ruthenium center toward the anionic cyclometalated ligand, which is directly connected to the IrO₂ catalyst through the malonate ligand. At the same time, the LUMO is shifted away from the IrO₂-bound cyclometalated ligand, toward the lower-lying bipyridine unoccupied states. A drawback of introducing such a chemical modification is however the shift at higher energies (i.e., less positive potentials vs NHE) of the dye oxidation potential due to the strong donor character of the anionic phenylpyridine ligand, which can however be tuned to some extent by ligand fluorination.¹²⁰

We have thus computationally assessed the performance of dye2 against the parent dye1 in the (e^-/h^+) transfer processes 2, 3, 6, and 5, see Figure 5a–d and the estimated injection rates in Table 2. Notably, the proposed chemical design improves both the probability function for electron and hole transfer rates to TiO₂ and IrO₂, Figure 5a–c, respectively, leading at the same time to its reduction for the dye excited-state quenching to IrO₂, Figure 5b. We also notice that hole injection into the IrO₂ catalyst could be made significantly more efficient if one were able to further down-shift the dye2 HOMOs, thus sampling a region of higher IrO₂ VB DOS, Figure 5c. In other words, the loss due to the negative (vs NHE) HOMO shift of dye2 compared to dye1 is partly compensated by the strong increase in the electronic coupling with the IrO₂ VB due to the ligand engineering, since the IrO₂ DOS is essentially unaltered by attachment of different dyes.

An overall picture of the energy levels of the complete TiO₂/dye/IrO₂ DSPEC photoanode for dye1 and dye2 is reported in Figure 6e,f. Notably, our computational approach quantitatively describes the expected energetics of the investigated DSPEC architecture, showing the dye HOMOs within the IrO₂ VB as well as the dye LUMOs distributed above the TiO₂ CB. As it can be noticed, the dye2 HOMOs show a considerably broader distribution than those of dye1, reflecting their stronger interaction with the IrO₂ VB, despite sampling a relatively lower IrO₂ VB DOS.

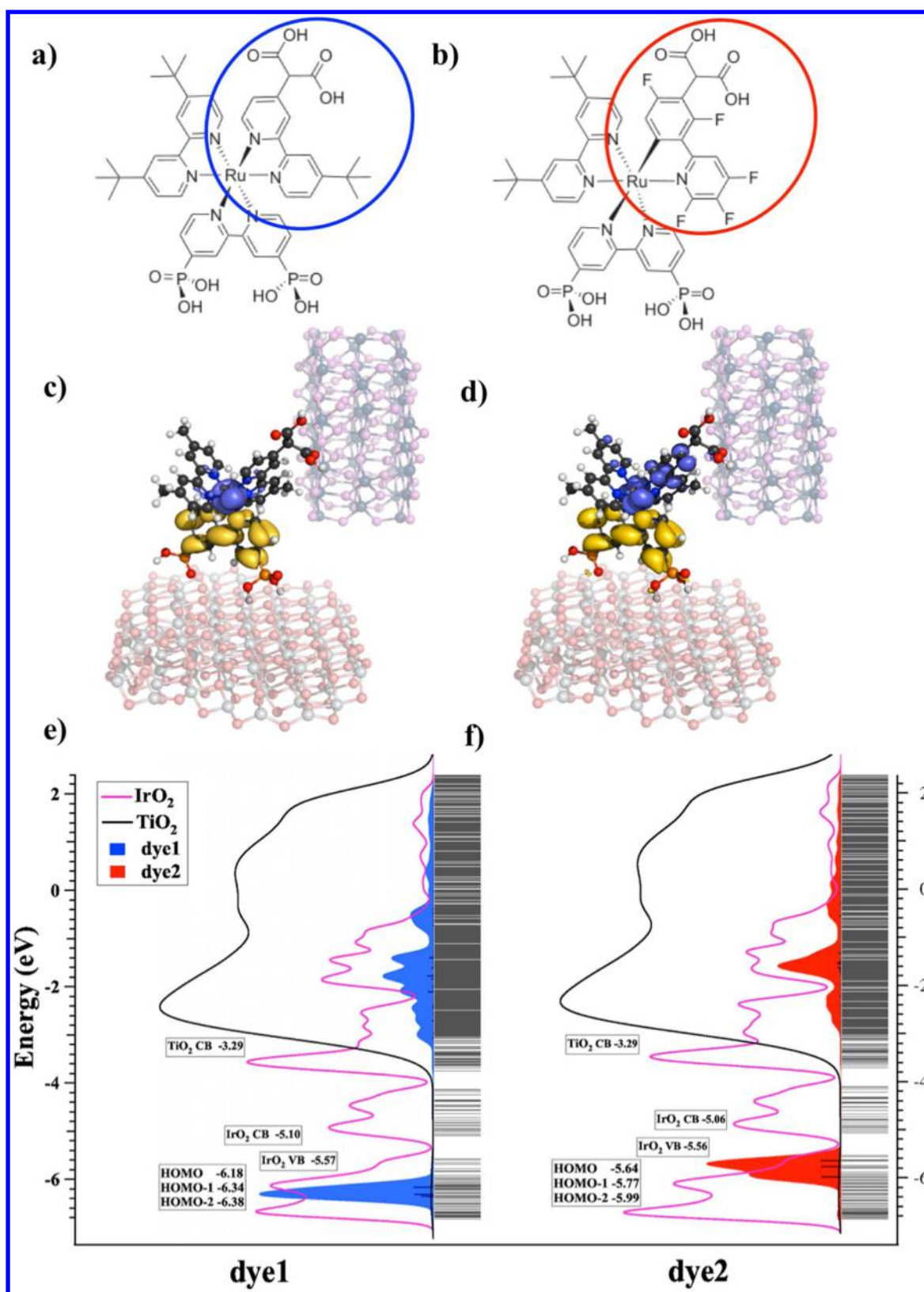


Figure 6. Molecular structure of dye1 (a) and of the cyclometalated Ru(II) dye2 (b) and their HOMO–LUMO density difference isosurfaces (blue and yellow lobes indicate density depletion and accumulation respectively) (c and d). (e and f) Alignment of energy levels in the $\text{TiO}_2/\text{dye}/\text{IrO}_2$ assemblies based on dye1 and dye2, respectively.

4. SUMMARY AND CONCLUSIONS

In summary, we have investigated for the first time, by state of the art computational modeling the crucial triple $\text{TiO}_2/\text{dye}/\text{IrO}_2$

heterointerface characterizing a typical DSPEC photoanode architecture for water splitting. We have considered a prototypical DSPEC,¹⁵ consisting of a bifunctional heteroleptic

Ru(II) sensitizer, showing phosphonate groups for TiO₂ anchoring and a malonate group to bind to hydrated iridium dioxide (IrO₂·nH₂O) nanoparticles. Our quantitative analysis of the critical electron/hole transfer rates based on extended models of the prototypical system has unveiled the crucial electronic features underlying the device functioning, highlighting the slow hole injection to IrO₂ and the fast parasitic dye excited-state quenching to IrO₂ as the major sources of the low device efficiency, fully in line with the experimental evidence.^{15,59} Based on this information, we have designed and computationally probed a new cyclometalated dye which showed globally improved interfacial properties compared to the parent dye, highlighting the possible design routes toward new and more efficient materials for water splitting.

■ ASSOCIATED CONTENT

■ Supporting Information

Comparison between calculated and experimental rates. Optimized geometrical structures. This material is available free of charge via the Internet at <http://pubs.acs.org>.

■ AUTHOR INFORMATION

Corresponding Authors

*chiara@thch.unipg.it

*filippo@thch.unipg.it

Notes

The authors declare no competing financial interest.

■ ACKNOWLEDGMENTS

We thank CNR-EFOR for partly funding this work. We thank Dr. Sergio Rampino and Dr. Enrico Ronca for providing us with data analysis computational tools.

■ REFERENCES

- (1) Grätzel, M. *Acc. Chem. Res.* **2009**, *42*, 1788–1798.
- (2) Young, K. J.; Martini, L. A.; Milot, R. L.; Snoeberger Iii, R. C.; Batista, V. S.; Schmittenmaer, C. A.; Crabtree, R. H.; Brudvig, G. W. *Coord. Chem. Rev.* **2012**, *256*, 2503–2520.
- (3) Hamann, T. W. *Nat. Mater.* **2014**, *13*, 3–4.
- (4) Concepcion, J. J.; House, R. L.; Papanikolas, J. M.; Meyer, T. J. *Proc. Natl. Acad. Sci. U.S.A.* **2012**, *109*, 15560–15564.
- (5) Fujishima, A.; Honda, K. *Nature* **1972**, *238*, 37–38.
- (6) Kato, H.; Asakura, K.; Kudo, A. *J. Am. Chem. Soc.* **2003**, *125*, 3082–3089.
- (7) Chen, X.; Shen, S.; Guo, L.; Mao, S. S. *Chem. Rev.* **2010**, *110*, 6503–6570.
- (8) Higashi, M.; Domen, K.; Abe, R. *Environ. Sci.* **2011**, *4*, 4138–4147.
- (9) Chen, Z.; Jaramillo, T. F.; Deutsch, T. G.; Kleiman-Shwarsstein, A.; Forman, A. J.; Gaillard, N.; Garland, R.; Takanabe, K.; Heske, C.; Sunkara, M.; McFarland, E. W.; Domen, K.; Miller, E. L.; Turner, J. A.; Dinh, H. N. *J. Mater. Res.* **2010**, *25*, 3–16.
- (10) Minggu, L. J.; Wan Daud, W. R.; Kassim, M. B. *Int. J. Hydrogen Energy* **2010**, *35*, 5233–5244.
- (11) Cristino, V.; Caramori, S.; Argazzi, R.; Meda, L.; Marra, G. L.; Bignozzi, C. A. *Langmuir* **2011**, *27*, 7276–7284.
- (12) Yang, J.; Wang, D.; Han, H.; Li, C. *Acc. Chem. Res.* **2013**, *46*, 1900–1909.
- (13) Higashi, M.; Domen, K.; Abe, R. *J. Am. Chem. Soc.* **2012**, *134*, 6968–6971.
- (14) Reece, S. Y.; Hamel, J. A.; Sung, K.; Jarvi, T. D.; Esswein, A. J.; Pijpers, J. J. H.; Nocera, D. G. *Science* **2011**, *334*, 645–648.
- (15) Youngblood, W. J.; Lee, S.-H. A.; Kobayashi, Y.; Hernandez-Pagan, E. A.; Hoertz, P. G.; Moore, T. A.; Moore, A. L.; Gust, D.; Mallouk, T. E. *J. Am. Chem. Soc.* **2009**, *131*, 926–927.
- (16) Youngblood, W. J.; Lee, S.-H. A.; Maeda, K.; Mallouk, T. E. *Acc. Chem. Res.* **2009**, *42*, 1966–1973.
- (17) Swierk, J. R.; Mallouk, T. E. *Chem. Soc. Rev.* **2013**, *42*, 2357–2387.
- (18) Gao, Y.; Zhang, L.; Ding, X.; Sun, L. *Phys. Chem. Chem. Phys.* **2014**, *16*, 12008–12013.
- (19) Moore, G. F.; Blakemore, J. D.; Milot, R. L.; Hull, J. F.; Song, H.-e.; Cai, L.; Schmittenmaer, C. A.; Crabtree, R. H.; Brudvig, G. W. *Energy Environ. Sci.* **2011**, *4*, 2389–2392.
- (20) Li, L.; Duan, L.; Xu, Y.; Gorlov, M.; Hagfeldt, A.; Sun, L. *Chem. Commun.* **2010**, *46*, 7307–7309.
- (21) Zhao, Y.; Swierk, J. R.; Megiatto, J. D.; Sherman, B.; Youngblood, W. J.; Qin, D.; Lentz, D. M.; Moore, A. L.; Moore, T. A.; Gust, D.; Mallouk, T. E. *Proc. Natl. Acad. Sci. U.S.A.* **2012**, *109*, 15612–15616.
- (22) Hanson, K.; Torelli, D. A.; Vannucci, A. K.; Brennaman, M. K.; Luo, H.; Alibabaei, L.; Song, W.; Ashford, D. L.; Norris, M. R.; Glasson, C. R. K.; Concepcion, J. J.; Meyer, T. J. *Angew. Chem., Int. Ed.* **2012**, *51*, 12782–12785.
- (23) Alibabaei, L.; Brennaman, M. K.; Norris, M. R.; Kalanyan, B.; Song, W.; Losego, M. D.; Concepcion, J. J.; Binstead, R. A.; Parsons, G. N.; Meyer, T. J. *Proc. Natl. Acad. Sci. U.S.A.* **2013**, *110*, 20008–20013.
- (24) Yu, Z.; Li, F.; Sun, L. *Energy Environ. Sci.* **2015**, *8*, 760–775.
- (25) Wu, L.-Z.; Chen, B.; Li, Z.-J.; Tung, C.-H. *Acc. Chem. Res.* **2014**, *47*, 2177–2185.
- (26) Li, G.; Sproviero, E. M.; Snoeberger Iii, R. C.; Iguchi, N.; Blakemore, J. D.; Crabtree, R. H.; Brudvig, G. W.; Batista, V. S. *Energy Environ. Sci.* **2009**, *2*, 230–238.
- (27) Wasylenko, D. J.; Palmer, R. D.; Berlinguette, C. P. *Chem. Commun.* **2013**, *49*, 218–227.
- (28) Klepser, B. M.; Bartlett, B. M. *J. Am. Chem. Soc.* **2014**, *136*, 1694–1697.
- (29) Berardi, S.; Drouet, S.; Francas, L.; Gimbert-Surinach, C.; Guttentag, M.; Richmond, C.; Stoll, T.; Llobet, A. *Chem. Soc. Rev.* **2014**, *43*, 7501–7519.
- (30) Wiechen, M.; Spiccia, L. *Chem. Catal. Chem.* **2014**, *6*, 439–441.
- (31) Yin, Q.; Tan, J. M.; Besson, C.; Geletii, Y. V.; Musaev, D. G.; Kuznetsov, A. E.; Luo, Z.; Hardcastle, K. I.; Hill, C. L. *Science* **2010**, *328*, 342–345.
- (32) Duan, L.; Araujo, C. M.; Ahlquist, M. S. G.; Sun, L. *Proc. Natl. Acad. Sci. U.S.A.* **2010**, *109*, 15584–15588.
- (33) Norris, M. R.; Concepcion, J. J.; Fang, Z.; Templeton, J. L.; Meyer, T. J. *Angew. Chem.* **2013**, *125*, 13825–13828.
- (34) Gao, Y.; Ding, X.; Liu, J.; Wang, L.; Lu, Z.; Li, L.; Sun, L. *J. Am. Chem. Soc.* **2013**, *135*, 4219–4222.
- (35) Duan, L.; Bozoglian, F.; Mandal, S.; Stewart, B.; Privalov, T.; Llobet, A.; Sun, L. *Nat. Chem.* **2012**, *4*, 418–423.
- (36) Lv, H.; Geletii, Y. V.; Zhao, C.; Vickers, J. W.; Zhu, G.; Luo, Z.; Song, J.; Lian, T.; Musaev, D. G.; Hill, C. L. *Chem. Soc. Rev.* **2012**, *41*, 7572–7589.
- (37) Kärkäs, M. D.; Verho, O.; Johnston, E. V.; Åkerman, B. *Chem. Rev.* **2014**, *114*, 11863–12001.
- (38) Kiwi, J.; Grätzel, M. *Angew. Chem., Int. Ed.* **1979**, *18*, 624–626.
- (39) Hara, M.; Waraksa, C. C.; Lean, J. T.; Lewis, B. A.; Mallouk, T. E. *J. Phys. Chem. A* **2000**, *104*, 5275–5280.
- (40) Blakemore, J. D.; Gray, H. B.; Winkler, J. R.; Müller, A. M. *ACS Catal.* **2013**, *3*, 2497–2500.
- (41) Jiao, F.; Frei, H. *Angew. Chem., Int. Ed.* **2009**, *48*, 1841–1844.
- (42) Osterloh, F. E. *Chem. Soc. Rev.* **2013**, *42*, 2294–2320.
- (43) Harriman, A.; Pickering, I. J.; Thomas, J. M.; Christensen, P. A. *J. Chem. Soc., Faraday Trans 1* **1988**, *84*, 2795–2806.
- (44) Lattach, Y.; Rivera, J. F.; Bamine, T.; Deronzier, A.; Moutet, J.-C. *ACS Appl. Mater. Interfaces* **2014**, *6*, 12852–12859.
- (45) Bledowski, M.; Wang, L.; Neubert, S.; Mitoraj, D.; Beranek, R. *J. Phys. Chem. C* **2014**, *118*, 18951–18961.
- (46) Swierk, J. R.; McCool, N. S.; Saunders, T. P.; Barber, G. D.; Strayer, M. E.; Vargas-Barbosa, N. M.; Mallouk, T. E. *J. Phys. Chem. C* **2014**, *118*, 17046–17053.
- (47) Zhao, Y.; Hernandez-Pagan, E. A.; Vargas-Barbosa, N. M.; Dysart, J. L.; Mallouk, T. E. *J. Phys. Chem. Lett.* **2011**, *2*, 402–406.

- (48) Swierk, J. R.; McCool, N. S.; Saunders, T. P.; Barber, G. D.; Mallouk, T. E. *J. Am. Chem. Soc.* **2014**, *136*, 10974–10982.
- (49) Suntivich, J.; May, K. J.; Gasteiger, H. A.; Goodenough, J. B.; Shao-Horn, Y. *Science* **2011**, *334*, 1383–1385.
- (50) Meyer, G. J. *Inorg. Chem.* **2005**, *44*, 6852–6864.
- (51) Griffith, M. J.; Sunahara, K.; Wagner, P.; Wagner, K.; Wallace, G. G.; Officer, D. L.; Furube, A.; Katoh, R.; Mori, S.; Mozer, A. J. *Chem. Commun.* **2012**, *48*, 4145–4162.
- (52) Martini, L. A.; Moore, G. F.; Milot, R. L.; Cai, L. Z.; Sheehan, S. W.; Schmuttenmaer, C. A.; Brudvig, G. W.; Crabtree, R. H. *J. Phys. Chem. C* **2013**, *117*, 14526–14533.
- (53) Swierk, J. R.; Méndez-Hernández, D. D.; McCool, N. S.; Liddell, P.; Terazono, Y.; Pahk, I.; Tomlin, J. J.; Oster, N. V.; Moore, T. A.; Moore, A. L.; Gust, D.; Mallouk, T. E. *Proc. Natl. Acad. Sci. U.S.A.* **2015**, *109*, 15612–15616.
- (54) Xiao, F.-X.; Miao, J.; Wang, H.-Y.; Yang, H.; Chen, J.; Liu, B. *Nanoscale* **2014**, *6*, 6727–6737.
- (55) Alibabaei, L.; Luo, H.; House, R. L.; Hoertz, P. G.; Lopez, R.; Meyer, T. J. *J. Mater. Chem. A* **2013**, *1*, 4133–4145.
- (56) Brimblecombe, R.; Koo, A.; Dismukes, G. C.; Swiegers, G. F.; Spiccia, L. *J. Am. Chem. Soc.* **2010**, *132*, 2892–2894.
- (57) Xiang, X.; Fielden, J.; Rodríguez-Córdoba, W.; Huang, Z.; Zhang, N.; Luo, Z.; Musaev, D. G.; Lian, T.; Hill, C. L. *J. Phys. Chem. C* **2013**, *117*, 918–926.
- (58) Fan, K.; Li, F.; Wang, L.; Daniel, Q.; Gabrielsson, E.; Sun, L. *Phys. Chem. Chem. Phys.* **2014**, *16*, 25234–25240.
- (59) Hoertz, P. G.; Kim, Y.-I.; Youngblood, W. J.; Mallouk, T. E. *J. Phys. Chem. B* **2007**, *111*, 6845–6856.
- (60) Lopez, A. M.; Natali, M.; Pizzoloto, E.; Chiorboli, C.; Bonchio, M.; Sartorel, A.; Scandola, F. *Phys. Chem. Chem. Phys.* **2014**, *16*, 12000–12007.
- (61) Pastore, M.; De Angelis, F. Modeling Materials and Processes in Dye-Sensitized Solar Cells: Understanding the Mechanism. *Improving the Efficiency*; Springer: Berlin Heidelberg, 2013; pp 1–86.
- (62) De Angelis, F. *Acc. Chem. Res.* **2014**, *47*, 3349–3360.
- (63) Sproviero, E. M.; Gascón, J. A.; McEvoy, J. P.; Brudvig, G. W.; Batista, V. S. *J. Am. Chem. Soc.* **2008**, *130*, 3428–3442.
- (64) Yang, X.; Hall, M. B. *J. Am. Chem. Soc.* **2009**, *132*, 120–130.
- (65) Mavros, M. G.; Tsuchimochi, T.; Kowalczyk, T.; McIsaac, A.; Wang, L.-P.; Voorhis, T. V. *Inorg. Chem.* **2014**, *53*, 6386–6397.
- (66) Sobolewski, A. L.; Domcke, W. *J. Phys. Chem. A* **2008**, *112*, 7311–7313.
- (67) Rivalta, I.; Brudvig, G. W.; Batista, V. S. Computational Studies of the Oxygen-Evolving Complex of Photosystem II and Biomimetic Oxomanganese Complexes for Renewable Energy Applications. In *Applications of Molecular Modeling to Challenges in Clean Energy*; American Chemical Society: Washington, DC, 2013; Vol. 1133, pp 203–215.
- (68) Sproviero, E. M.; Shinopoulos, K.; Gascón, J. A.; McEvoy, J. P.; Brudvig, G. W.; Batista, V. S. *Philosophical Transactions of the Royal Society B: Biological Sciences* **2008**, *363*, 1149–1156.
- (69) Vittadini, A.; Selloni, A.; Rotzinger, F. P.; Grätzel, M. *Phys. Rev. Lett.* **1998**, *81*, 2954–2957.
- (70) Lundqvist, M. J.; Nilsing, M.; Persson, P.; Lunel, S. *Int. J. Quantum Chem.* **2006**, *106*, 3214–3234.
- (71) De Angelis, F.; Fantacci, S.; Mosconi, E.; Nazeeruddin, M. K.; Grätzel, M. *J. Phys. Chem. C* **2011**, *115*, 8825–8831.
- (72) Pastore, M.; Selloni, A.; Fantacci, S.; Angelis, F. Electronic and Optical Properties of Dye-Sensitized TiO₂ Interfaces. In *Topics in Current Chemistry*; Springer: Berlin Heidelberg, 2014; pp 1–45.
- (73) te Velde, G.; Bickelhaupt, F. M.; Baerends, E. J.; Fonseca Guerra, C.; van Gisbergen, S. J. A.; Snijders, J. G.; Ziegler, T. *J. Comput. Chem.* **2001**, *22*, 931–967.
- (74) Becke, A. D. *Phys. Rev. A* **1988**, *38*, 3098–3100.
- (75) Perdew, J. P. *Phys. Rev. B* **1986**, *33*, 8822–8824.
- (76) Cossi, M.; Rega, N.; Scalmani, G.; Barone, V. *J. Comput. Chem.* **2003**, *24*, 669–681.
- (77) Barone, V.; Cossi, M. *J. Phys. Chem. A* **1998**, *102*, 1995–2001.
- (78) Frisch, M. J.; Trucks, G. W.; Schlegel, H. B.; Scuseria, G. E.; Robb, M. A.; Cheeseman, J. R.; Scalmani, G.; Barone, V.; Mennucci, B.; Petersson, G. A.; Nakatsuji, H.; Caricato, M.; Li, X.; Hratchian, H. P.; Izmaylov, A. F.; Bloino, J.; Zheng, G.; Sonnenberg, J. L.; Hada, M.; Ehara, M.; Toyota, K.; Fukuda, R.; Hasegawa, J.; Ishida, M.; Nakajima, T.; Honda, Y.; Kitao, O.; Nakai, H.; Vreven, T.; Montgomery, J. A., Jr.; Peralta, J. E.; Ogliaro, F.; Bearpark, M.; Heyd, J. J.; Brothers, E.; Kudin, K. N.; Staroverov, V. N.; Kobayashi, R.; Normand, J.; Raghavachari, K.; Rendell, A.; Burant, J. C.; Iyengar, S. S.; Tomasi, J.; Cossi, M.; Rega, N.; Millam, N. J.; Klene, M.; Knox, J. E.; Cross, J. B.; Bakken, V.; Adamo, C.; Jaramillo, J.; Gomperts, R.; Stratmann, R. E.; Yazyev, O.; Austin, A. J.; Cammi, R.; Pomelli, C.; Ochterski, J. W.; Martin, R. L.; Morokuma, K.; Zakrzewski, V. G.; Voth, G. A.; Salvador, P.; Dannenberg, J. J.; Dapprich, S.; Daniels, A. D.; Farkas, Ö.; Foresman, J. B.; Ortiz, J. V.; Cioslowski, J.; Fox, D. J. *Gaussian 09*, revision D.1; Gaussian, Inc.: Wallingford, CT, 2009.
- (79) Dunning, T. H. J.; Hay, P. J. *Modern Theoretical Chemistry*; Plenum: New York; 1977; Vol. 3.
- (80) Hay, P. J.; Wadt, W. R. *J. Chem. Phys.* **1985**, *82*, 299–310.
- (81) Wadt, W. R.; Hay, P. J. *J. Chem. Phys.* **1985**, *82*, 284–298.
- (82) Hay, P. J.; Wadt, W. R. *J. Chem. Phys.* **1985**, *82*, 270–283.
- (83) Kondov, I.; Čížek, M.; Benesch, C.; Wang, H.; Thoss, M. *J. Phys. Chem. C* **2007**, *111*, 11970–11981.
- (84) Li, J.; Wang, H.; Persson, P.; Thoss, M. *J. Chem. Phys.* **2012**, *137*, 22A529–516.
- (85) Agrawal, S.; Leijtens, T.; Ronca, E.; Pastore, M.; Snaith, H.; De Angelis, F. *J. Mater. Chem. A* **2013**, *1*, 14675–14685.
- (86) Ronca, E.; Marotta, G.; Pastore, M.; De Angelis, F. *J. Phys. Chem. C* **2014**, *118*, 16927–16940.
- (87) de Almeida, J. S.; Ahuja, R. *Phys. Rev. B* **2006**, *73*, 165102.
- (88) Miao, M. S.; Seshadri, R. *J. Phys.: Condens. Matter* **2012**, *24*, 215503.
- (89) Clancy, J. P.; Chen, N.; Kim, C. Y.; Chen, W. F.; Plumb, K. W.; Jeon, B. C.; Noh, T. W.; Kim, Y.-J. *Phys. Rev. B* **2012**, *86*, 195131.
- (90) Hirata, Y.; Ohgushi, K.; Yamaura, J.-i.; Ohsumi, H.; Takeshita, S.; Takata, M.; Arima, T.-h. *Phys. Rev. B* **2013**, *87*, 161111.
- (91) Kahl, J. M.; Poll, C. G.; Oropeza, F. E.; Ablett, J. M.; Céolin, D.; Rueff, J.-P.; Agrestini, S.; Utsumi, Y.; Tsuei, K. D.; Liao, Y. F.; Borgatti, F.; Panaccione, G.; Regoutz, A.; Egdel, R. G.; Morgan, B. J.; Scanlon, D. O.; Payne, D. J. *Phys. Rev. Lett.* **2014**, *112*, 117601.
- (92) Goodenough, J. B. *J. Solid. State Chem.* **1971**, *3*, 490–500.
- (93) Riga, J.; Tenret-Noël, C.; Pireaux, J. J.; Caudano, R.; Verbist, J. J.; Gobillon, Y. *Phys. Scri.* **1977**, *16*, 351.
- (94) Gambardella, A. A.; Bjorge, N. S.; Alspaugh, V. K.; Murray, R. W. *J. Phys. Chem. C* **2011**, *115*, 21659–21665.
- (95) Frame, F. A.; Townsend, T. K.; Chamousis, R. L.; Sabio, E. M.; Ditttrich, T.; Browning, N. D.; Osterloh, F. E. *J. Am. Chem. Soc.* **2011**, *133*, 7264–7267.
- (96) Kavan, L.; Grätzel, M.; Gilbert, S. E.; Klemenz, C.; Scheel, H. J. *J. Am. Chem. Soc.* **1996**, *118*, 6716–6723.
- (97) Pechy, P.; Rotzinger, F. P.; Nazeeruddin, M. K.; Kohle, O.; Zakeeruddin, S. M.; Humphry-Baker, R.; Grätzel, M. *J. Chem. Soc. Chem. Comm.* **1995**, 65–66.
- (98) Zakeeruddin, S. M.; Nazeeruddin, M. K.; Pechy, P.; Rotzinger, F. P.; Humphry-Baker, R.; Kalyanasundaram, K.; Grätzel, M.; Shklover, V.; Haibach, T. *Inorg. Chem.* **1997**, *36*, 5937–5946.
- (99) Zabir, H.; Gillaizeau, I.; Bignozzi, C. A.; Caramori, S.; Charlot, M.-F.; Cano-Boquera, J.; Odobel, F. *Inorg. Chem.* **2003**, *42*, 6655–6666.
- (100) Gillaizeau-Gauthier, I.; Odobel, F.; Alebbi, M.; Argazzi, R.; Costa, E.; Bignozzi, C. A.; Qu, P.; Meyer, G. J. *Inorg. Chem.* **2001**, *40*, 6073–6079.
- (101) Bae, E.; Choi, W.; Park, J.; Shin, H. S.; Kim, S. B.; Lee, J. S. *J. Phys. Chem. B* **2004**, *108*, 14093–14101.
- (102) Hanson, K.; Brennaman, M. K.; Luo, H.; Glasson, C. R. K.; Concepcion, J. J.; Song, W.; Meyer, T. J. *ACS Appl. Mater. Interfaces* **2012**, *4*, 1462–1469.
- (103) Luschtinetz, R.; Frenzel, J.; Milek, T.; Seifert, G. *J. Phys. Chem. C* **2009**, *113*, 5730–5740.

- (104) Nilsing, M.; Lunell, S.; Persson, P.; Ojamäe, L. *Surf. Sci.* **2005**, *582*, 49–60.
- (105) Lundqvist, M. J.; Nilsing, M.; Lunell, S.; Åkerman, B.; Persson, P. *J. Phys. Chem. B* **2006**, *110*, 20513–20525.
- (106) Guerrero, G.; Mutin, P. H.; Vioux, A. *Chem. Mater.* **2001**, *13*, 4367–4373.
- (107) Pawsey, S.; Yach, K.; Reven, L. *Langmuir* **2002**, *18*, 5205–5212.
- (108) Lafont, U.; Simonin, L.; Gaberscek, M.; Kelder, E. M. *J. Phys. Chem. C* **2007**, *111*, 1104–1108.
- (109) Nilsing, M.; Persson, P.; Lunell, S.; Ojamäe, L. *J. Phys. Chem. C* **2007**, *111*, 12116–12123.
- (110) Nilsing, M.; Persson, P.; Ojamäe, L. *Chem. Phys. Lett.* **2005**, *415*, 375–380.
- (111) Pang, C. L.; Watkins, M.; Cabailh, G.; Ferrero, S.; Ngo, L. T.; Chen, Q.; Humphrey, D. S.; Shluger, A. L.; Thornton, G. *J. Phys. Chem. C* **2010**, *114*, 16983–16988.
- (112) Coppens, P.; Chen, Y.; Trzop, E. *Chem. Rev.* **2014**, *114*, 9645–9661.
- (113) De Angelis, F.; Fantacci, S.; Selloni, A. *Nanotechnology* **2008**, *19*, 424002.
- (114) She, C.; Guo, J.; Irle, S.; Morokuma, K.; Mohler, D. L.; Zabri, H.; Odobel, F.; Youm, K.-T.; Liu, F.; Hupp, J. T.; Lian, T. *J. Phys. Chem. A* **2007**, *111*, 6832–6842.
- (115) Bessho, T.; Yoneda, E.; Yum, J.-H.; Guglielmi, M.; Tavernelli, I.; Imai, H.; Rothlisberger, U.; Nazeeruddin, M. K.; Grätzel, M. *J. Am. Chem. Soc.* **2009**, *131*, 5930–5934.
- (116) Bomben, P. G.; Koivisto, B. D.; Berlinguette, C. P. *Inorg. Chem.* **2010**, *49*, 4960–4971.
- (117) Colombo, A.; Dragonetti, C.; Valore, A.; Coluccini, C.; Manfredi, N.; Abboto, A. *Polyhedron* **2014**, *82*, 50–56.
- (118) Schulze, B.; Brown, D. G.; Robson, K. C. D.; Friebe, C.; Jäger, M.; Birckner, E.; Berlinguette, C. P.; Schubert, U. S. *Chem.—Eur. J.* **2013**, *19*, 14171–14180.
- (119) Chitumalla, R. K.; Gupta, K. S. V.; Malapaka, C.; Fallahpour, R.; Islam, A.; Han, L.; Kotamarthi, B.; Singh, S. P. *Phys. Chem. Chem. Phys.* **2014**, *16*, 2630–2640.
- (120) De Angelis, F.; Fantacci, S.; Evans, N.; Klein, C.; Zakeeruddin, S. M.; Moser, J.-E.; Kalyanasundaram, K.; Bolink, H. J.; Grätzel, M.; Nazeeruddin, M. K. *Inorg. Chem.* **2007**, *46*, 5989–6001.